



Morphological evolution of 3D ZnO hierarchical nanostructures by diethylene glycol-assisted sol–gel synthesis for highly effective photocatalytic performance

Hoai Linh Pham^{1,2} · Van Hao Nguyen³ · Van Khien Nguyen³ · Nhu Hoa Thi Tran^{4,5} · Hong Phong Thi Le¹ · Thi Huong Tran¹ · Hong Nhung Nguyen¹ · Kieu Giang Thi Lam¹ · Van Thanh Dang⁶

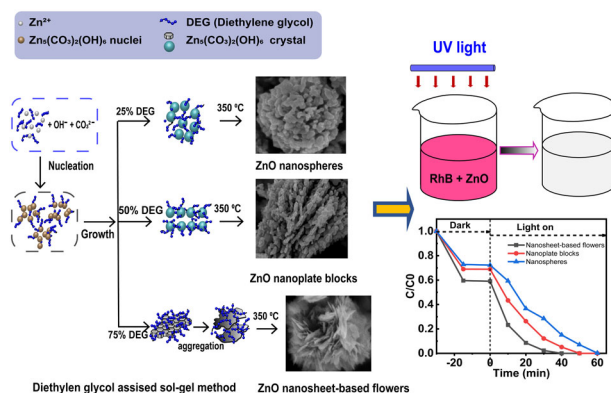
Received: 25 December 2021 / Accepted: 17 June 2022 / Published online: 14 July 2022

© The Author(s), under exclusive licence to Springer Science+Business Media, LLC, part of Springer Nature 2022, corrected publication 2022

Abstract

In this study, we focus on synthesizing various 3D ZnO hierarchical nanostructures (ZnH) for highly effective photocatalytic performance via an innovative sol-gel method using diethylene glycol as an assembly-guiding agent. The morphology of 3D ZnH can be turned from nanospheres into nanoplate blocks and nanosheet-based flowers by increasing the concentration of diethylene glycol. Possible growth mechanisms are proposed for different assembly architectures. Analysis of characterization techniques reveal that the synthesized hierarchical structures exhibited a large specific surface area, high degree of crystallinity, and a band gap in the range 2.95–3.11 eV, depending on their morphology. X-ray photoelectron and photoluminescence spectroscopy revealed the presence of rich oxygen vacancies introduced by the 3D ZnO hierarchical morphology. The photodegradation experiment results presented in ZnO nanosheet-based flower shown superior photoactivity of rhodamine B degradation compared with nanospheres and nanoplate blocks structures. This is attributed to the larger surface area, enhanced light absorption, and more effective photogenerated charge separation on account of their rich Vo. The establishment of relevant structural–optical property relationships is expected to provide deeper insights into the potential use of ZnH for innovative devices.

Graphical abstract



✉ Hoai Linh Pham
linhph@ims.vast.ac.vn

¹ Institute of Materials Science, Vietnam Academy of Science and Technology, Hanoi, Vietnam

² Graduate University of Science and Technology, Vietnam Academy of Science and Technology, Hanoi, Vietnam

³ Institute of Science and Technology, TNU—University of Sciences, Thai Nguyen, Vietnam

⁴ Faculty of Materials Science and Technology, University of Science, Ho Chi Minh City, Vietnam

⁵ Vietnam National University, Ho Chi Minh City, Vietnam

⁶ TNU—University of Medicine and Pharmacy, Thai Nguyen, Vietnam

Keywords ZnO · Hierarchical structures · Optical properties · Sol–gel method

Highlights

- Three different 3D ZnO hierarchical nanostructures were successfully synthesized.
- The morphology-optical properties relationship of the obtained samples was studied.
- Optical properties and oxygen defects are dependent on 3D ZnO hierarchical morphology.
- The ZnO nanosheet-based flowers exhibit excellent photocatalytic activity.

1 Introduction

ZnO nanomaterials are well known to be important semiconductors with unique chemical and physical properties; as such, these materials have great potential applications in photocatalysts, solar cells, and sensors, optoelectronic devices [1]. Reviews of the structural, crystal growth methods, and fundamental properties of ZnO nanomaterials have revealed that the superior electronic structure and optical properties of ZnO depend on its morphology and structure [2–4]. Therefore, controlling the morphology of ZnO nanomaterials, especially their size and shape, is an area of active interest in materials science. To date, ZnO nanomaterials with a wide variety of structures and morphologies, including 1D (particles and nanowires/tubes), 2D (nanosheets, belts, and plates), and 3D (nanospheres and flowers) hierarchical structures, have been produced using various chemical methods [3–9]. Among the numerous structures, ZnO hierarchical nanostructures (ZnH) exhibit many outstanding advantages. These nanostructures not only inherit the excellent properties of assembled low-dimensional nanomaterials but also offer advanced properties for the design of superior active catalysts, ultra-sensitive sensors, and highly effective adsorption materials for various applications [10, 11]. In this context, methods to develop facile approaches to fabricate ZnH with a unique oxygen vacancy (V_o)-rich structure are a prominent research subject [11–13]. Oxygen surface defects in ZnO crystals are considered important because they enhance optical absorption and charge generation and separation, thereby promoting improved ZnO performance [12, 14, 15]. Although different approaches have been employed to synthesize these structures [16], delivering a relatively inexpensive, clean, and simple method to produce nanostructures on a large scale with desirable features, including well-controlled size, morphology, porosity, oxygen defects, and electronic band structure, remains challenging [17]. Moreover, reports on the correlation between the hierarchical morphology and optical properties of 3D ZnH, as well as the effects of V_o defects on their photocatalytic performance, are scarce.

Using surfactants such as diethylene glycol (DEG) as an agent for the self-assembly of hierarchical ZnO is an

appealing way for 3D structure construction reported in the pieces of literature [18, 19]. DEG is well known as a cheap surfactant with glycols that have strong affinity for water which plays an important role in the formation of the hierarchical structures. Thus, by adjusting the volume ratio of DEG and water can vary the 3D morphology of ZnH. Therefore, in this study, we present a simple, and scalable sol–gel approach to synthesize ZnH with various morphologies by using DEG used as a structure-directing and capping agent. The correlation between the morphology and optical properties of ZnH, particularly their light absorption, band gap, photo-induced charge separation and recombination, V_o concentration, and photocatalytic activity were investigated in detail.

2 Experimental

2.1 Preparation of ZnO hierarchical nanostructures

ZnO samples were synthesized via a sol–gel method under the assistance of diethylene glycol as an assembling agent. Typically, 13.6 g of zinc acetate dihydrate (98%, Sigma-Aldrich) was poured into 100 mL of a mixed solvent of DEG (99%, Sigma-Aldrich) and water with the help of a magnetic stirring for 1 h. Thereafter, 140 ml of carbonate solution (1.5 M, 98%, Sigma-Aldrich) was added dropwise into the above solution and remained stirring within 1 h at room temperature. The reaction product was washed with distilled water until neutral (pH 7) and then dried in an oven for 24 h at 60 °C. After drying, the white precipitate was heated at 350 °C for 2 h with the initial heating rate of 10 °C/min and then cooled down to room temperature. The concentration of DEG was varied by changing the volume ratio of DEG/water to 25% (25 mL/75 mL), 50% (50 mL/50 mL), and 75% (75 mL/25 mL), corresponding to the samples named Z25%, Z50%, and Z75%, respectively.

2.2 Characterization

X-ray diffraction (XRD—Bruker D8 Advance) measurements to determine the crystal structure of as-prepared samples and the field emission scanning electron microscopy

(FE-SEM; Hitachi S-4800) was used to analyze their morphology. Microstructures were identified by high-resolution transmission electron microscopy (HRTEM; JEM 2100, JEOL). X-ray photoelectron spectroscopy (XPS - Mutilab-2000 spectrometer) was performed to determine the chemical composition of the samples. The Brunauer–Emmett–Teller (BET) surface area and Barrett–Joyner–Halenda (BJH) porous size distribution of the samples were estimated from the N_2 adsorption–desorption isotherms obtained using a Micromeritics 3Flex surface characterization analyzer. UV–vis NIR absorption spectrophotometer (Hitachi U-4100) and FLS-1000 PL spectrometer (Edinburgh Instruments) were employed to investigate optical absorption and photoluminescence (PL) spectra.

2.3 Photocatalytic activity test

Photocatalytic experiments were performed by dispersing 30 mg of catalyst into 60 mL of an aqueous solution of RhB (5 ppm) under stirring in the dark for 30 min to achieve adsorption–desorption equilibrium, the suspension then was exposed to UV-light irradiation provided by a Philips UVC 15 W. The distance from the light source to the liquid level of the RhB aqueous solution maintained at 25 cm. During the photoreaction, 2 mL of the RhB solution containing ZnO samples was collected at 10 min intervals and centrifuged at 9500 rpm for 8 min to remove the catalyst. The degradation process of RhB was monitored by measuring the absorbance of RhB at 554 nm using a UV–Vis spectrometer (Jasco V-670). The residual concentration of the RhB solution was estimated by absorption spectroscopy measurement at 554 nm through the calibration curve of the relationship between the absorbance intensity and RhB concentration.

3 Results and discussion

3.1 Structural, morphological characterizations

Figure 1a presents the XRD patterns of the ZnO samples synthesized with different DEG concentrations. The diffraction peaks of the three samples display at angles that match with were in good agreement with the characteristic peaks of the hexagonal wurtzite structure of ZnO (PDF card number 01-075-6445) without any impurities. The sharp peaks in the XRD patterns demonstrate that the ZnO samples are well crystallized and oriented. A magnification of the XRD pattern (Fig. 1b) reveals that the diffraction peaks broaden and shift toward higher 2θ angles with increasing DEG concentration; this finding implies that the crystallite size and lattice constant of the ZnO samples decrease with increasing DEG concentration.

Interestingly, the (0 0 2) peak of the Z75% sample is stronger than those of the Z25% and Z50% samples and standard JCPDS data. The relative intensities of (1 0 0) to (0 0 2) in the ZnO samples decrease from 1.269 to 1.09 and 0.99 with increasing DEG concentration, thereby indicating that the (0 0 2) face orients toward the growth of ZnO as the DEG concentration increases. Similar observations of the increasing intensity of the (0 0 2) peak as the morphology of the ZnO crystals changes from nanoparticles and nanorods to nanosheets have been reported in the literature [20, 21]. The different morphologies of the as-prepared ZnO nanostructures lead to variations in their XRD pattern, as confirmed by the FESEM images.

Figure 2 shows the FESEM images of the ZnO samples synthesized with different DEG concentrations. All of the samples exhibit well-defined hierarchical nanostructures in the form of nanospheres, nanoplate blocks, and special flower structures, corresponding to DEG concentrations of 25% (Z25%), 50% (Z50%), and 75% (Z75%), respectively. The morphology of the nanostructures changes drastically with increasing DEG concentration. At a low DEG concentration of 25%, individual ZnO nanoparticles of ~10–40 nm assemble to form nanospheres with a diameter of ~400 nm. Continuous increases in DEG concentration to 50% result in smaller ZnO particles in the range of 10–20 nm that tend to align in plates that stack to build nanoplate blocks. When the DEG concentration is further increased to 75%, a uniform spherical morphology of flowers constructed by ultrathin ZnO nanosheets with a uniform thickness of several nanometers is formed; the ZnO nanosheets intersect with each other to form multilayer petals of flower structures measuring 400–600 nm in diameter. The morphological evolution of the samples shows that DEG promotes the self-assembly of ZnO nanoparticles at low concentrations to form a nanospherical morphology. At higher concentrations, DEG acts as a structure-directing and capping agent that restricts the growth of ZnO crystals and helps them grow in the preferential direction, resulting in decreases in crystalline size and the formation of nanoplates and nanosheets [22].

HRTEM images were obtained, as shown in Fig. 2c, f, i to identify the crystal facets of the ZnO samples. The HRTEM images of all samples exhibit well-resolved lattice fringes, thereby indicating the high crystallinity of the ZnO structures with the interplanar spacing samples of 0.52, 0.517, and 0.515 nm for Z25%, Z50%, and Z75%, respectively, which could be assigned to the (0001) plane [20, 23]. The Z75% sample also exhibits a lattice d-spacing of 2.87 nm, which corresponds to the $\{10\bar{1}0\}$ plane of hexagonal-phase ZnO. These results indicate that the ZnO crystals of the Z25% and Z50% samples growth along the [0001] plane to form particle structures. The preferential

Fig. 1 X-ray diffraction patterns of ZnO nanomaterials synthesized with different DEG concentrations

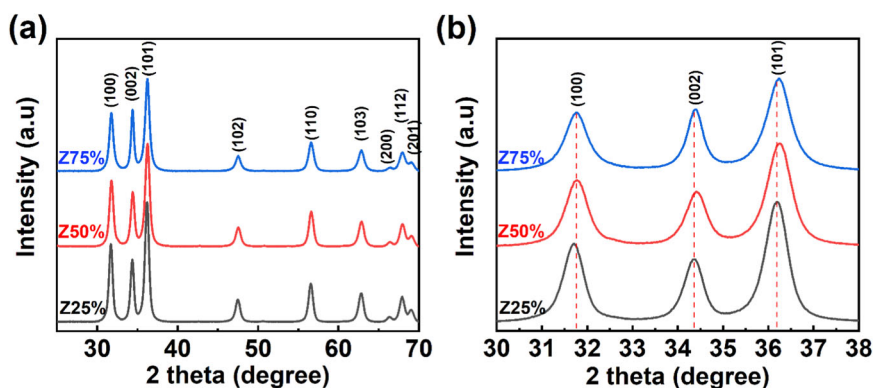
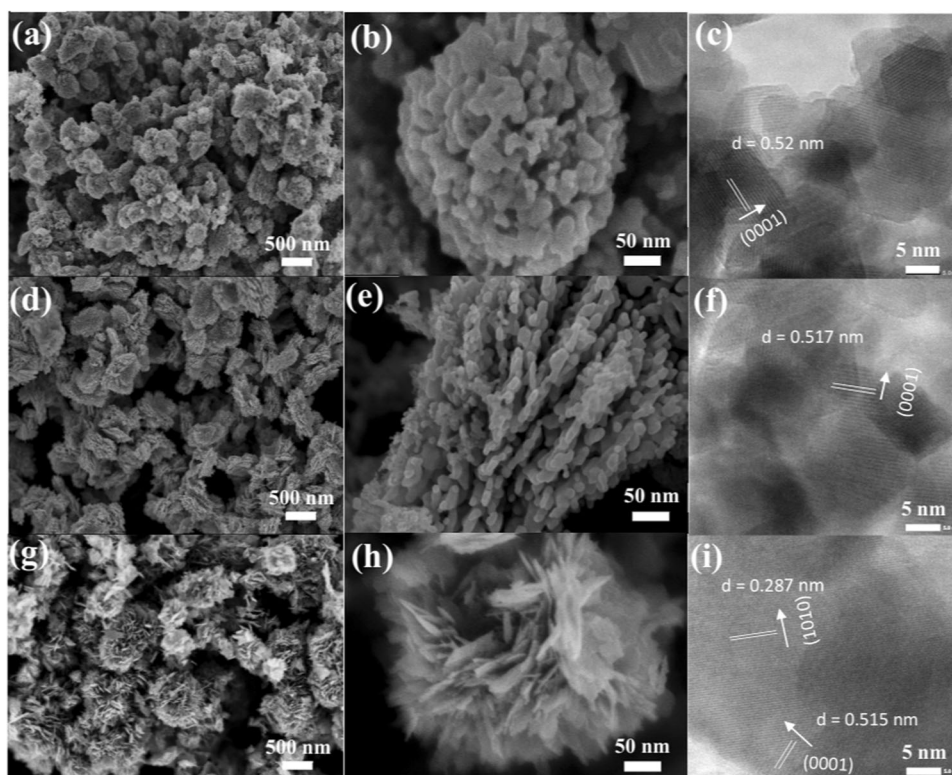


Fig. 2 Low/high-magnification FESEM images and HRTEM images of ZnO hierarchical nanostructures synthesized with different DEG concentrations: **a–c** Z25%, **d–f** Z50%, and **g–i** Z75%

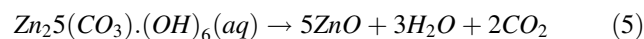
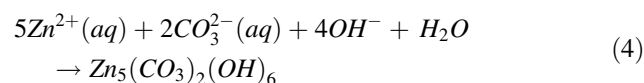
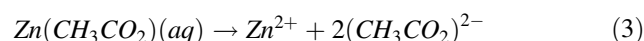
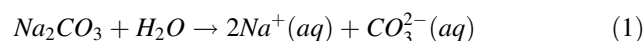


growth plane of the Z75% sample is in the (0001) and $\{01\bar{1}0\}$ directions, thus forming nanosheets on the initial ZnO nuclei [24].

3.2 Formation mechanism of different ZnO hierarchical morphologies

The formation mechanism of ZnH is based on the crystal growth process of ZnO and the assembly process of the ZnO crystals. According to ref. [25], the formation of ZnO nanostructures through the reaction of carbonate-based reducing agents is a complex process involving intermediates including $Zn(OH)_2$, $[Zn(OH)_4]_2$, $ZnCO_3$, and $Zn_5(CO_3)_2(OH)_6$. The possible formation mechanism of different ZnO hierarchical morphologies in our work may

be described by the following chemical reactions:



At high reactant concentrations, intermediates are formed by a burst of initial homogeneous nucleation, and

Fig. 3 Schematic illustration of a possible mechanism of the formation of ZnO hierarchical nanostructures

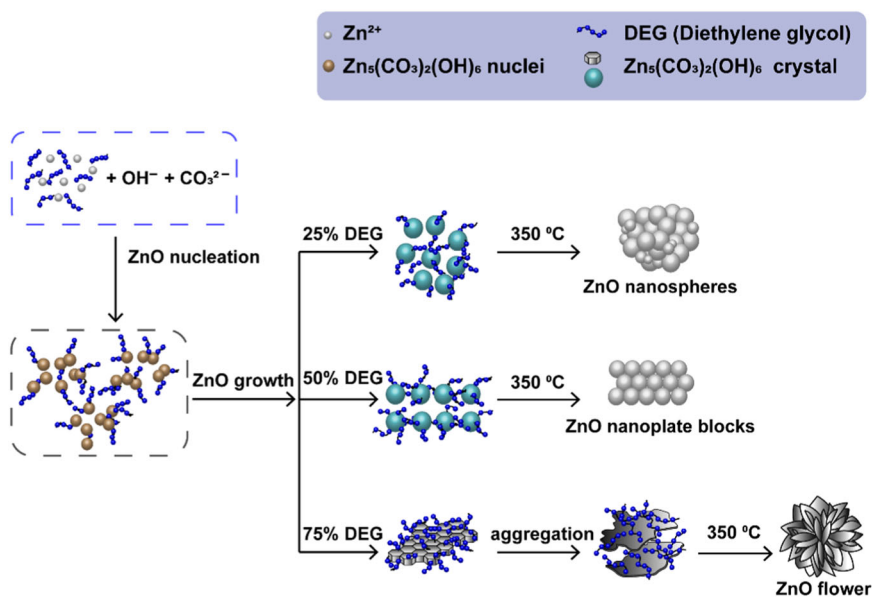
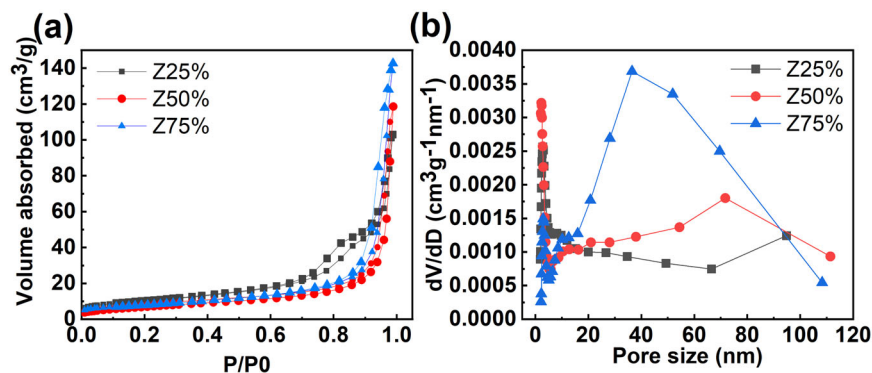


Fig. 4 **a** N₂ adsorption–desorption curves and **b** BJH pore size distribution curves of ZnO hierarchical nanostructures



Zn₅(CO₃)₂(OH)₆ crystal nuclei are formed via the crystalline processes and phase transformation of amorphous intermediates. The nuclei formed move until they achieve the required crystallographic orientation and accumulate by lateral atom-by-atom addition on other particles, resulting in anisotropic growth [25, 26]. The ZnO nanostructures are finally formed by dehydration of Zn₅(CO₃)₂(OH)₆ crystal nuclei. ZnO crystals are well known to possess two polar planes, including the positive Zn-terminated (0001) plane and the negative polar O-ZnO (000 $\bar{1}$) plane. Previous research has reported that ZnO crystallites grow rapidly along the [0001] direction of the *c*-axis to form nanowires or nanorods on account of the high surface energy of the (0001) plane, which renders it more active than other planes. The presence of DEG not only strongly influences the rate of atom deposition on different crystal faces but also controls the rate of ZnO crystal growth [27]. When Zn₅(CO₃)₂(OH)₆ crystal nuclei form, the DEG molecules in the solution absorb and occupy some of the active sites of the ZnCO₃ hydroxide crystal nuclei [28]. Interactions between DEG

molecules via H-bonds may affect the orientation and growth of the nuclei, as well as the assembly of crystal particles [29]. At low concentrations, DEG molecules act as bridges that bind nuclei particles to create crystal agglomerations, and the ZnO particles formed retain their spherical morphology; this supposition indicates that no preferential growth axis could be observed at low DEG concentrations. At high DEG concentrations, however, the increased ratio of DEG molecules adsorbed on the surface of the nuclei inhibits the growth units of primary particles, especially along the *c*-axis. However, interactions between DEG molecules still play an important role in linking growth units in the preferred direction of the non-polar faces of ZnO crystals to produce both nanoplates and nanosheets. A possible mechanism for the formation of ZnH is illustrated in Fig. 3.

3.3 Surface area and oxygen defects in ZnO samples

To better understand the BET surface area and porous nature of ZnH with different morphologies, the adsorption–desorption

isotherms in N_2 were carried out and shown in Fig. 4. The adsorption–desorption isotherms of the three samples exhibit a type IV curve with H_2 hysteresis loops for the Z25% sample and H_3 hysteresis loops for the Z50% and Z75% samples, corresponding to hollow- and parallel plate-shaped pores. The ZnH displays large specific surface areas, with values estimated to be 30.5, 34.7, and 48.1 m^2/g for nanospheres, nanoplate blocks, and flowers, respectively. Compared with that 1D ZnO nanoparticles, the specific surface area of ZnH is 3–5 times greater [2]. The BJH pore size distributions (Fig. 4b) indicate that all of the samples possess a mesoporous morphology with bimodal pore distributions, one in the range of 1–5 nm and another in the range of 5–120 nm. The pore volumes of the Z25%, Z50%, and Z75% samples are calculated to be 0.190837, 0.185720, and 0.22035 cm^3/g , respectively.

High-resolution O 1s XPS spectra were measured, as shown in Fig. 5, to obtain information about the Vo of the ZnO hierarchical nanostructures. Thermo-Fisher Advantage version 4.88 software was used to fit the XPS data of

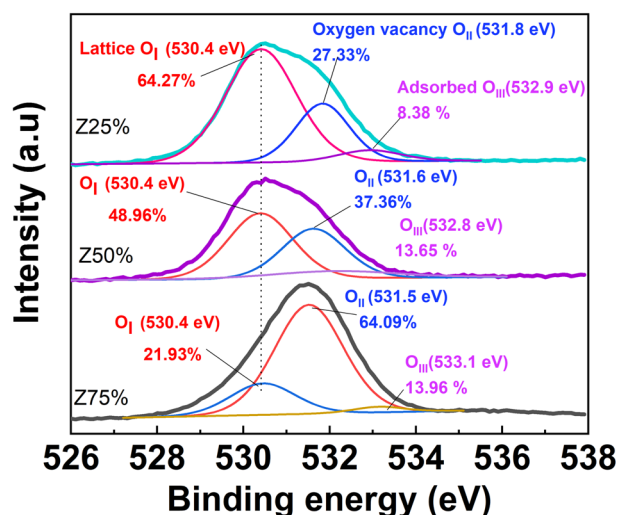


Fig. 5 High-resolution O1s XPS spectra of ZnO hierarchical nanostructures synthesized with different DEG concentrations

all samples to a Gaussian distribution. The O 1s XPS profiles of all samples could be deconvoluted into three peaks, namely O_I, O_{II}, and O_{III}. The peak areas of O_I, O_{II}, and O_{III} for all samples are listed in Table 1. The first O_I peak centered at ~530.4 eV is attributed to O²⁻ ions binding to Zn²⁺ ions in the wurtzite structure of ZnO, which means O_I represents the O²⁻ ions in the ZnO lattice [30]. The third O_{III} peak centered at 533 eV could be assigned to oxygen adsorbed on the ZnO surface, including O₂, hydroxyl (OH⁻), and carbonate (CO₃²⁻) groups [31]. The second peak O_{II} centered at ~531.6 eV originates from oxygen ions in oxygen-deficient regions caused by Vo on the ZnO surface. As known, the intensity of the O_{II} peak is closely related to the density of Vo [32]. Therefore, the concentration of Vo in the ZnO samples could be studied via the O_{II} peak. Integration of the peak area results reveals that the contribution ratios of the O_{II} peak in the O1s XPS spectra of spherical, nanoplate blocks, and nanosheet-based flowers ZnO are 27.33%, 37.36%, and 64.09%, respectively. These results indicate that a greater number of oxygen atoms escape the ZnO nanosheet-based flower crystals, leaving V_O defects, than the other morphologies. The Vo concentration in the as-prepared ZnH is also higher than that in other ZnO nanostructures reported in recent literature [33–35]. The high concentration of Vo introduced in ZnH may improve their charge separation efficiency, resulting in enhanced photocatalytic activity [36].

3.4 Optical properties and photocatalytic activity

Figure 6 shows the UV–vis diffuse reflectance spectra of the ZnH with different morphologies. All of the samples exhibit absorption bands at ~400 nm, which corresponds to the intrinsic band gap absorption of ZnO. Compared with that of nanospherical structures, the absorption band of nanoplate blocks is blue-shifted while that of flower structures is red-shifted. These results suggest that the flower structures show enhanced light absorption; the

Table 1 Fitting results of the O 1s XPS spectra of various ZnO hierarchical nanostructures into different oxygen species: (O_I, O_{II}, O_{III}), Binding energy (E_B), Relative percentage (R), Time constant (τ)

Samples	Morphology	Oxygen species	E_B (eV)	R (%)	τ_1 (ns)	τ_2 (ns)
Zn25%	Spherical particles	O _I	530.4	64.27	1.827	9.2
		O _{II}	531.8	27.33		
		O _{III}	533.02	8.38		
Zn50%	Nanoplate blocks	O _I	530.4	48.96	1.92	10.04
		O _{II}	531.6	37.36		
		O _{III}	532.8	13.65		
Zn75	Nanosheet-based flowers	O _I	530.4	21.93	1.92	13.6
		O _{II}	531.5	64.09		
		O _{III}	533.2	13.96		

high porosity of interlaced nanosheets may promote the trapping of incident light within this type of structure. The band gaps of the nanospheres, nanoplate blocks, and flower structures were estimated by the τ_c equation as follows [37]:

$$(ah\nu)^{1/\gamma} = B(h\nu - E_g) \quad (6)$$

where B is a constant called the band tailing parameter, ν is the photon frequency, h is the Planck constant, E_g is the band gap energy, and γ is a power factor of the transition mode that depends on the nature of the material ($\gamma = 1/2$ or 2 for direct and indirect transition band gaps, respectively). By extrapolating a straight line in a certain region of the $(ah\nu)^2$ versus $h\nu$ curve to the zero ordinate, the band gaps of nanospheres, nanoplate blocks, and flower structures could be estimated to be 3.08, 3.11, and 2.95 eV, respectively. Changes in the band gaps of the ZnH further confirm that ZnO hierarchical morphology

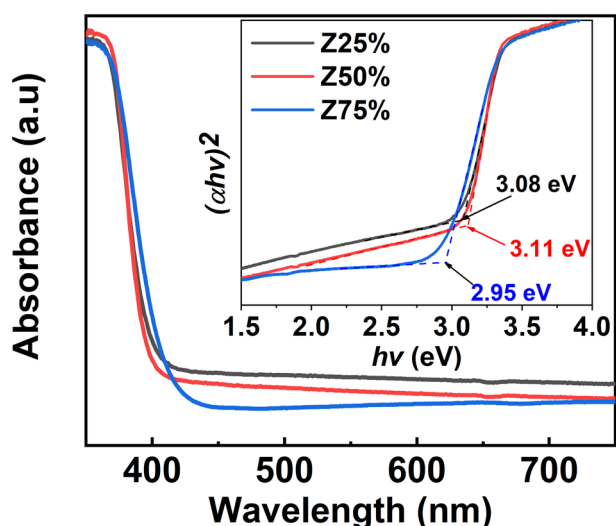
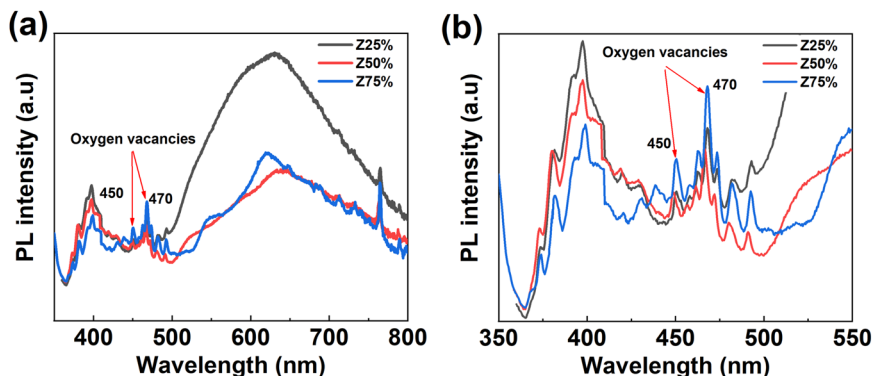


Fig. 6 UV-vis diffuse reflectance spectra and the corresponding Tauc plots of the as-prepared samples (inset)

Fig. 7 **a** Room-temperature PL spectra of ZnO hierarchical nanostructures with different morphologies, **b** The enlarged PL spectra of ZnO hierarchical nanostructures at wavelengths from 350 nm to 550 nm



results in an effective band gap, which is smaller than its bulk value of 3.37 eV. The narrowed band gap of the ZnH could be related to an increase in Vo concentration, as revealed by the XPS spectra [31].

Information on photogenerated electron-hole separation and recombination and the introduction of Vo to the various ZnH were investigated by PL spectroscopy at an excitation wavelength of 340 nm. Figure 7 illustrates the PL spectra of the different 3D ZnH. All of the samples exhibit two major emission regions a UV emission band and a visible emission band. UV emission with a peak centered at ~398 nm could be ascribed to the intrinsic emission of ZnO, which is produced by electron transitions from the conduction band to the valence band of ZnO. Visible emission is related to the impurity energy of defects in the ZnO crystal caused by Vo (with peaks at ~447 and 470 nm) [36, 38], interstitial zinc (with a peak centered at 420 nm), interstitial oxygen (with a peak centered at 570 nm), zinc vacancies, and anti-site oxygen (with a peak centered at 660 nm) [14, 36, 39]. The relative Vo concentration in the 3D ZnH could be estimated by comparing the intensity of blue peaks at 470 nm in the PL spectra [40]. Figure 7 clearly shows that the intensity of peaks assigned to Vo shows the order Z75% > Z50% > Z25%; the highest peak appears in the sample with flower nanostructures, thus reflecting the large number of Vo defects in these structures. Vo emissions are related to the radiative recombination of an electron occupying the Vo with a photo-generated hole [41]. The decrease in peak intensity at 400 nm may be due to the Vo defect in the ZnO nanostructures associated with trapping sites which are caused by the reduced recombination of the photo-generated e-h pairs, as confirmed by the reduction in the intensity of the peak at 400 nm [14]. According to Fig. 6, the peak intensity at 400 nm is lowest in the flower samples and relatively higher in the nanoplate block and spherical samples. These results indicate that ZnO nanosheet-based flowers, which feature the highest Vo concentration among the samples obtained, exhibit the best

separation of photo-induced electron–hole pairs, which greatly improve photocatalytic properties.

Time-resolved PL spectroscopy was conducted using a pulsed laser with an energy of 363 nm to discriminate between emissive states and the exciton lifetime, which is directly related to electron–hole recombination and defects in the ZnH. Figure 8 shows the time-resolved PL spectra of three ZnH samples. The TRPL data of all

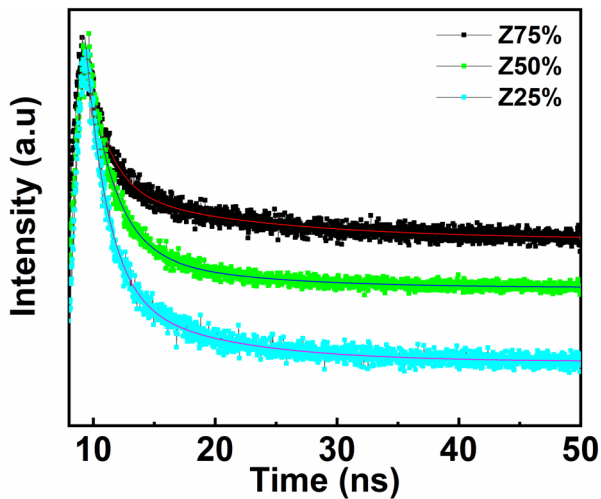


Fig. 8 TRPL spectra of ZnO hierarchical nanostructure with different morphologies

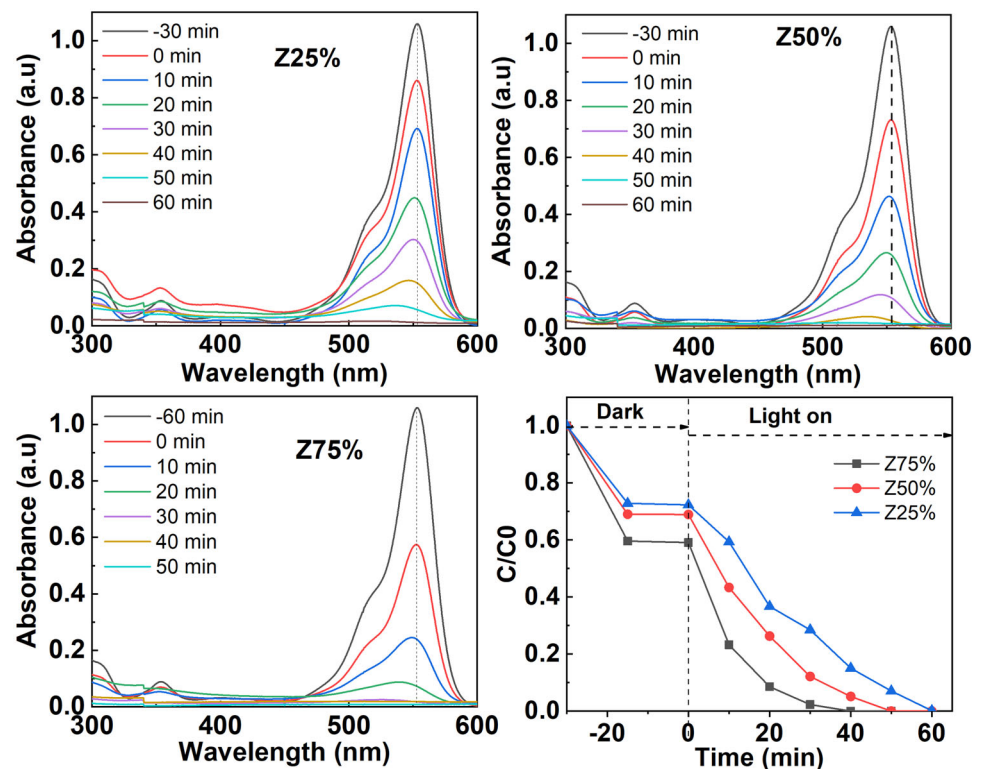
samples were well-fitted by a bi-exponential model:

$$I = I_1 \exp\left(-\frac{t}{\tau_1}\right) + I_2 \exp\left(-\frac{t}{\tau_2}\right) \quad (7)$$

$$\tau_{avg} = \frac{I_1 \tau_1^2 + I_2 \tau_2^2}{I_1 \tau_1 + I_2 \tau_2} \quad (8)$$

where I_1 and I_2 are the decay amplitudes, τ_1 is a fast time constant originates from the direct radiative recombination of photo-generated carriers from valence–conduction band [42]; and τ_2 is a slow time constant related to indirect electron–hole recombination at localizing level of defects such as oxygen vacancies, interstitial zinc that act as the initial charge carriers acceptor to inhibit electron/hole recombination [43]. The time constants obtained from the fitting results are listed in Table 1. The slow time component of ZnO nanosheet-based flowers is longer than that of other morphologies, thus confirming the higher level of trapping sites in these nanostructures. The XPS and PL spectra reveal that the Vo concentration is also highest in the ZnO nanosheet-based flowers, thus indicating that Vo plays an important role in capturing photogenerated electrons in the ZnH. The average electron lifetimes of the ZnO nanospheres, nanoplate blocks, and nanosheet-based flowers are calculated to be 1.99, 2.2, and 2.39 ns, respectively. The long lifetime of photogenerated charge carriers found in the ZnH implies effective charge carrier

Fig. 9 a–c UV–vis spectra of the residual RhB solution under different UV irradiation times in the presence of three ZnO samples. **d** Photodegradation curve of RhB in the presence of three ZnO samples



separation, which could improve the photocatalytic activity of the samples.

The photocatalytic activity of ZnH was studied via the degradation of RhB solution under UV light irradiation. A plot of the residual RhB concentration as a function of irradiation time is presented in Fig. 8d. As shown in Fig. 9, the photocatalytic activity of the ZnH depends on their morphology. The ZnO nanosheet-based flowers showed the highest RhB degradation efficiency, completely decomposing the RhB solution within 30 min of irradiation. Among the ZnO materials tested, the ZnO nanospheres display the lowest photocatalytic activity, degrading 100% RhB only after 60 min. The higher photocatalytic activity of ZnO flowers compared with those of other nanostructures may be related to the following: i) the large surface area of the flowers could provide a greater amount of surface-active agents for the degradation of pollutant molecules; ii) the high concentration of oxygen defects effectively suppresses electron–hole recombination, as confirmed by the quenching of the PL intensity of the ZnO flowers; and iii) enhanced light absorption helps increase electron–hole separation. These effects could contribute to

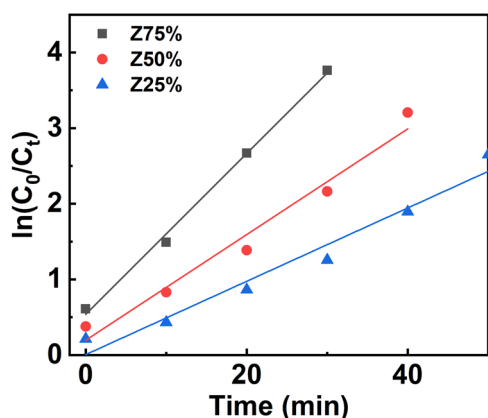


Fig. 10 Linear fitting $\ln(C_0/C_t)$ vs. t of the kinetic curves for RhB degradation under UV light irradiation

the high activity of flower-like ZnO nanomaterials, which may be applied to wastewater treatment.

The initial degradation rate of RhB was further explored by calculating the photodegradation reaction rate constant based on the reaction kinetics curves of pseudo-first-order reaction as the following equation [44]:

$$\ln(C_0/C_t) = kt \quad (9)$$

where C_0 is the initial concentration of RhB solution, C_t is the concentration of RhB solution at irradiation time t (min), k (min^{-1}) is the reaction rate constant of RhB degradation. By linear fitting of $\ln(C_0/C_t)$ against time for all samples (as shown in Fig. 10), the photodegradation rate constant k was obtained to be 0.1063 min^{-1} , 0.06986 min^{-1} , 0.04846 min^{-1} for g-Z75%, Z50%, and Z25%, respectively. Taking the results together, ZnH is worthy of further study as photocatalysts with greater efficiency compared with those described in previous reports (Table 2) [45–48].

4 Conclusion

In summary, nanospheres, nanoplate blocks, and nano-flowers were successfully synthesized by using a simple sol–gel method with DEG as an assembly-guiding agent. DEG acts as a structure-directing agent that could promote or restrict the growth of ZnO crystals, resulting in different hierarchical morphologies. The morphology of the obtained nanostructures greatly influenced their photocatalytic activity on account of the different effects of their light absorption, surface area, and oxygen defects. ZnO nanosheet-based flowers offered better photocatalytic performance than nanospheres and nanoplate blocks owing to their enhanced light absorption and higher surface area. The flowers also contain a high concentration of Vo. This indicated that, compared with other ZnO morphologies, oxygen atoms in the nanosheet-based flowers can easily escape creating a larger number of Vo defects.

Table 2 Comparison of the photocatalytic activities of ZnO nanosheet-based flowers with hierarchical ZnO nanostructures for RhB photodegradation in terms of light source (LS), photocatalyst concentration (C_p), RhB concentration (C_{RhB}), irradiation time (t_{Time}), and photocatalytic efficiency (E_{ff})

Photocatalyst	Light Source (UV)	C_p (mg/ml)	C_{RhB} (ppm)	t_{Time} (min)	E_{ff}	Ref
ZnO nanosheet-based flowers	a philips 15 W	0.5	5	30	100%	Our work
ZnO hierarchical nanostructures	125 W mercury lamp	10/15	10	100	63%	[45]
ZnO hexagonal platforms	Three Philips 15 W mercury lamps	300	2.5	60	42%	[46]
3D ZnO hierarchical nanostructures	UV light	0.2	10	100	78%	[47]
ZnO microflowers	500 W Hg lamp	1	10	100	100%	[48]

Data availability

The data used to support the findings of this study are included in the article.

Acknowledgements This research is funded by Vietnam National Foundation for Science and Technology Development (NAFOSTED) under grant number 103.02-2018.319.

Author contributions PHL: Conceptualization, Supervision, Writing - Original Draft, Funding acquisition. Resources, NVH: Data curation, Methodology, Investigation, NVK: Methodology, Investigation, LTHP: Conceptualization, Formal analysis, TTH: Formal analysis, Data Curation, Nguyen THN: Methodology, Validation, LTK Giang: Investigation, TTNK: Formal analysis, NVH: Writing—Review & Editing, DVT: Review & Editing.

Compliance with ethical standards

Conflict of interest The authors declare no competing interests.

Publisher's note Springer Nature remains neutral with regard to jurisdictional claims in published maps and institutional affiliations.

Springer Nature or its licensor holds exclusive rights to this article under a publishing agreement with the author(s) or other rightsholder(s); author self-archiving of the accepted manuscript version of this article is solely governed by the terms of such publishing agreement and applicable law.

References

- Theerthagiri J, Salla S, Senthil RA, Nithyadharseni P, Madankumar, Arunachalam P, Maiyalagan T, Kim H-S (2019) A review on ZnO nanostructured materials: energy, environmental and biological applications. *Nanotechnology* 30:392001–3920028. <https://doi.org/10.1088/1361-6528/ab268a>
- Lin Y, Hu H, Hu YH (2020) Role of ZnO morphology in its reduction and photocatalysis. *Appl Surf Sci* 502:144202. <https://doi.org/10.1016/j.apsusc.2019.144202>
- Iglesias-Juez A, Vines F, Lamiel-García O, Fernandez-García M, Illas F (2015) Morphology effects in photoactive ZnO nanostructures: photooxidative activity of polar surfaces. *J Mater Chem A* 3:8782–8792. <https://doi.org/10.1039/C5TA01111F>
- Yuan YF, Tu JP, Wu HM, Li Y, Shi DQ (2005) Size and morphology effects of ZnO anode nanomaterials for Zn/Ni secondary batteries. *Nanotechnology* 16:803–808. <https://doi.org/10.1088/1361-6528/ab268a>
- Hsu CL, Chang SJ (2014) Doped ZnO 1D nanostructures: synthesis, properties, and photodetector application. *Small* 10:4562–4585. <https://doi.org/10.1002/sml.201401580>
- Iqbal T, Khan MA, Mahmood Hasan (2018) Facile synthesis of ZnO nanosheets: structural, antibacterial and photocatalytic studies. *Mater Lett* 224:59–63. <https://doi.org/10.1016/j.matlet.2018.04.078>
- Shen J, Zhuang H, Wang D, Xue C, Liu H (2009) Growth and characterization of ZnO nanoporous belts. *Cryst Growth Des* 9:2187–2190. <https://doi.org/10.1021/cg800847d>
- Qi L, Li H, Dong L (2013) Simple synthesis of flower-like ZnO by a dextran assisted solution route and their photocatalytic degradation property. *Mater Lett* 107:354–356. <https://doi.org/10.1016/j.matlet.2013.06.054>
- Zhu C, Lu B, Su Q, Xie E, Lan W (2012) A simple method for the preparation of hollow ZnO nanospheres for use as a high-performance photocatalyst. *Nanoscale* 4:3060–3064. <https://doi.org/10.1039/C2NR12010K>
- Zhang H, Wu R, Chen Z, Liu G, Zhang Z, Jiao Z (2012) Self-assembly fabrication of 3D flower-like ZnO hierarchical nanostructures and their gas sensing properties. *CrystEngComm* 14:1775–1782. <https://doi.org/10.1039/C1CE06163A>
- Alenezi MR (2018) Hierarchical zinc oxide nanorings with superior sensing properties. *Mater Sci Eng: B*, 236–237:132–138. <https://doi.org/10.1016/j.mseb.2018.11.011>
- Liua F, Wang X, Chen X, Song X, Tian J, Cui H (2019) Porous ZnO ultrathin nanosheets with high specific surface areas and abundant oxygen vacancies for acetylacetone gas sensing. *ACS Appl. Mater. Interfaces* 27(11):24757–24763. <https://doi.org/10.1021/acsaami.9b06701>
- Wang J, Chen R, Xiang L, Komarneni S (2018) Synthesis, properties and applications of ZnO nanomaterials with oxygen vacancies: a review. *Ceram Int* 44:7357–7377. <https://doi.org/10.1016/j.ceramint.2018.02.013>
- Yu F, Liu Z, Li Y, Nan D, Wang B, He L, Zhang J, Tang X, Duan H, Liu Y (2020) Effect of oxygen vacancy defect regeneration on photocatalytic properties of ZnO nanorods. *Appl Phys A* 126:931–943. <https://doi.org/10.1007/s00339-020-04117-w>
- Baek M, Kim D, Yong K (2017) Simple but effective way to enhance photoelectrochemical solar-water-splitting performance of ZnO nanorod arrays: charge-trapping Zn(OH)₂ annihilation and oxygen vacancy generation by vacuum annealing. *ACS Appl Mater Interfaces* 9:2317–2325. <https://doi.org/10.1021/acsami.6b12555>
- Xia Y, Wang J, Chen R, Zhou D, Xiang L (2016) A review on the fabrication of hierarchical ZnO nanostructures for photocatalysis application. *Crystals* 6:148–167. <https://doi.org/10.3390/cryst6110148>
- Wang X, Ahmad M, Sun H (2017) Three-dimensional ZnO hierarchical nanostructures: solution phase synthesis and applications. *Materials* 10:1304–1328. <https://doi.org/10.3390/ma10111304>
- Taya YY, Li S, Boey F, Cheng YH, Liang MH (2007) Growth mechanism of spherical ZnO nanostructures synthesized via colloid chemistry. *Physica B* 394:372–376. <https://doi.org/10.1016/j.physb.2006.12.062>
- Saito N, Haneda H (2011) Hierarchical structures of ZnO spherical particles synthesized solvothermally. *Sci Technol Adv Mater* 12:064707–064714. <https://doi.org/10.1088/1468-6996/12/6/064707>
- Wang M, Zhang Y, Zhou Y, Yang F, Kim EJ, Hahn SH, Seong SG (2013) Rapid room-temperature synthesis of nanosheet-assembled ZnO mesocrystals with excellent photocatalytic activity. *CrystEngComm* 15:754–764. <https://doi.org/10.1039/c2ce26660a>
- Manzano CV, Caballero-Calero O, Hormeño S, Penedo M, Luna M, Martín-González MS (2013) ZnO morphology control by pulsed electrodeposition. *J Phys Chem C* 117:1502–1508. <https://doi.org/10.1021/jp3107099>
- Taheri M, Abdizadeh H, Golobostanfard MR (2018) Hierarchical ZnO nanoflowers and Urchin-like shapes synthesized via sol-gel electrophoretic deposition with enhanced photocatalytic performance. *Mater Chem Phys* 220:118–127. <https://doi.org/10.1016/j.matchemphys.2018.08.043>
- Zhou Y, Wang J, Zhou H, Xiang F, Yang H, Cai X, Liao H, Gua L, Wang Y (2019) Electrochemical approach towards the controllable synthesis of highly ordered and hierarchical zinc oxide dendritic crystal composed of hexagonal nanosheets: some insights into the stacking-assembly of hierarchical architecture. *CrystEngComm* 21:3919–3929. <https://doi.org/10.1039/C9CE00342H>

24. Krishnapriya R, Praneetha S, Murugan AV (2015) Energy-efficient, microwave-assisted hydro/solvothermal synthesis of hierarchical flowers and rice grain-like ZnO nanocrystals as photoanodes for high performance dye-sensitized solar cells. *CrystEngComm* 17:8353–8367. <https://doi.org/10.1039/C5CE01438G>
25. Barhoum A, Melcher J, Assche GV, Rahier H, Bechelany M, Fleisch M, Bahnemann D (2017) Synthesis, growth mechanism, and photocatalytic activity of Zinc oxide nanostructures: porous microparticles versus nonporous nanoparticles. *J Mater Sci* 52:2746–2762. <https://doi.org/10.1007/s10853-016-0567-3>
26. Wang F, Wang X (2014) Mechanisms in the solution growth of free-standing two-dimensional inorganic nanomaterials. *Nanoscale* 6:6398–6414. <https://doi.org/10.1039/C4NR00973H>
27. Songa R-Q, Colfen H (2011) Additive controlled crystallization. *CrystEngComm* 13:1249–1276. <https://doi.org/10.1039/C0CE00419G>
28. Dakhlaoui A, Jendoubi M, Smiri LS, Kanaev A, Jouini N (2009) Synthesis, characterization and optical properties of ZnO nanoparticles with controlled size and morphology. *J Cryst Growth* 311:3989–3996. <https://doi.org/10.1016/j.jcrysgro.2009.06.028>
29. Han H, Ni Y, Sheng E (2015) ZnO Nanoplates assembled by rod-like nanoparticles: Simple reflux synthesis, affecting factors and shape evolution towards nanorings. *RSC Adv* 5:51750–51761. <https://doi.org/10.1039/C5RA06203A>
30. Mun BS, Liu Z, Motin MA, Roy PC, Kim CM (2018) In situ observation of H₂ dissociation on the ZnO(0001) surface under high pressure of hydrogen using ambient-pressure XPS. *Int J Hydrog Energ* 43:8655–8661. <https://doi.org/10.1016/j.ijhydene.2018.03.155>
31. Wang J, Wang Z, Huang B, Ma Y, Liu Y, Qin X, Zhang X, Dai Y (2012) Oxygen vacancy induced band-gap narrowing and enhanced visible light photocatalytic activity of ZnO. *ACS Appl Mater Interfaces* 4:4024–4030. <https://doi.org/10.1021/am300835p>
32. Kotsisa K, Staemmler V (2006) Ab initio calculations of the O1s XPS spectra of ZnO and Zn oxo compounds. *Phys Chem Chem Phys* 8:1490–1498. <https://doi.org/10.1039/B515699H>
33. Li Q, Chen D, Miao J, Lin S, Yu Z, Cui D, Yang Z, Chen X (2021) Highly sensitive sensor based on ordered porous ZnO nanosheets for ethanol detecting application. *Sens Actuators B Chem* 326:128952–128962. <https://doi.org/10.1016/j.snb.2020.128952>. Volume, 1 January
34. Zhang Y-H, Li Y-L, Gong F-L, Xie K-F, Liu M, Zhang H-L, Fang S-M (2020) Al doped narcissus-like ZnO for enhanced aNO₂ sensing performance: an experimental and DFT investigation. *Sens Actuators B Chem* 305:127489–127497. <https://doi.org/10.1016/j.snb.2019.127489>
35. Qin S, Tang P, Feng Y, Li D (2020) Novel ultrathin mesoporous ZnO-SnO₂ n-n heterojunction nanosheets with high sensitivity to ethanol. *Sens Actuators B* 309:127801–127814. <https://doi.org/10.1016/j.snb.2020.127801>
36. Wang C, Wu D, Wang P, Ao Y, Hou J, Qian J (2015) Effect of oxygen vacancy on enhanced photocatalytic activity of reduced ZnO nanorod arrays. *Appl Surf Sci* 325:112–116. <https://doi.org/10.1016/j.apsusc.2014.11.003>
37. Makuła P, Michał Pacia, Macyk W (2018) How to correctly determine the band gap energy of modified semiconductor photocatalysts based on UV-Vis spectra. *J Phys Chem Lett* 9:6814–6817. <https://doi.org/10.1021/acs.jpcclett.8b02892>
38. Zhang DH, Xue ZY, Wang QP (2002) The mechanisms of blue emission from ZnO films deposited on glass substrate by r.f. magnetron sputtering. *J Phys D: Appl Phys* 35:2837–2840. <https://doi.org/10.1088/0022-3727/35/21/321>
39. Xu F, Lu Y, Xie Y, Liu Y (2009) Synthesis and photoluminescence of assembly-controlled ZnO architectures by aqueous chemical growth. *J Phys Chem C* 113:1052–1059. <https://doi.org/10.1021/jp808456r>
40. Fang J, Fan H, Ma Y, Wang Z, Chang Q (2015) Surface defects control for ZnO nanorods synthesized by quenching and their anti-recombination in photocatalysis. *Appl Surf Sci* 332:47–54. <https://doi.org/10.1016/j.apsusc.2015.01.139>
41. Fujihara S, Ogawa Y, Kasai A (2004) Tunable visible photoluminescence from ZnO thin films through Mg-doping and annealing. *Chem Mater* 16:2965–2968. <https://doi.org/10.1021/cm049599i>
42. Chebil W, Fouzri A, Fargi A, Azeza B, Zaaoub Z, Sallet V (2015) Characterization of ZnO thin films grown on different p-Si substrate elaborated by sol-gel spin-coating method. *Mater Res Bull* 70:719–727
43. Li H, Shang J, Ai Z, Zhang L (2015) Efficient visible light nitrogen fixation with BiOBr nanosheets of oxygen vacancies on the exposed {001} facets. *J Am Chem Soc* 137:6393–6399. <https://doi.org/10.1021/jacs.5b03105>
44. Hasija V, Sudhaik A, Raizada P, Hosseini-Bandegharai A, Singh P (2019) Carbon quantum dots supported AgI/ZnO/phosphorus-doped graphitic carbon nitride as Z-scheme photocatalyst for efficient photodegradation of 2,4-dinitrophenol. *J Environ Chem Eng* 7:103272–103284. <https://doi.org/10.1016/j.jece.2019.103272>
45. Kumari V, Yadav S, Jindal J, Sharma S, Kumari K, Kumar N (2020) Synthesis and characterization of heterogeneous ZnO/CuO hierarchical nanostructures for photocatalytic degradation of organic pollutant. *Adv Powder Technol* 7:2658–2668. <https://doi.org/10.1016/j.apt.2020.04.033>
46. Giraldi TR, Santos GVF, deMendonca VR, Ribeiro C, Weber IT (2012) Effect of synthesis parameters on the structural characteristics and photocatalytic activity of ZnO. *Mater Chem Phys* 136:505–511. <https://doi.org/10.1016/j.matchemphys.2012.07.018>
47. Mujtaba J, Sun H, Fang F, Ahmad M, Zhu J (2015) Fine control over the morphology and photocatalytic activity of 3D ZnO hierarchical nanostructures: capping vs. etching. *RSC Adv* 5:56232–56238. <https://doi.org/10.1039/C5RA08325G>
48. Guo Y, Lin S, Li X, Liu Y (2016) Amino acids assisted hydrothermal synthesis of hierarchically structured ZnO with enhanced photocatalytic activities. *Appl Surf Sci* 384:83–91. <https://doi.org/10.1016/j.apsusc.2016.04.036>